Demonstration of Dual-Channel TOPS SAR Imaging With Airborne C-Band Data

Huaitao Fan, Zhimin Zhang, Robert Wang, *Senior Member, IEEE*, Ning Li, *Member, IEEE*, Wei Xu, and Zhen Xu

Abstract—Multichannel in azimuth synthetic aperture radar (SAR) operating in the terrain observation by progressive scans (TOPS) acquisition mode has attracted much attention recently for its capability to achieve ultrawide-swath imaging with a high spatial resolution. In order to verify the feasibility and operability of this newly developed remote sensing concept, a C-band airborne azimuth dual-channel TOPS SAR has been designed by the Institute of Electronics, Chinese Academy of Sciences, as a test bed for future spaceborne realizations. This paper introduces the experimental SAR system and reports the data processing results of an outfield experiment conducted in late September 2014. The importance of the experiment resides in its potential to validate several important technical aspects of this novel SAR operation with real experimental data, including channel mismatch cancellation and unambiguous signal reconstruction. Besides, two kinds of processing methods are proposed to calibrate the influence of antenna phase center fluctuation occurred in the dual-channel TOPS SAR. Finally, the experimental results obtained, including the phase mismatch cancellation and the focused imageries, are presented and analyzed.

Index Terms—High-resolution wide-swath (HRWS) imaging, multichannel in azimuth synthetic aperture radar (SAR), terrain observation by progressive scans (TOPS).

I. Introduction

IN THE synthetic aperture radar (SAR) community, imaging of a continuous wide unambiguous swath has been one of the most important features for better observation of the dynamic process on the surface of the earth [1], [2]. Future spatial missions, such as vegetation mapping, soil moisture determination, and maritime domain surveillance, will necessitate a complete and frequent coverage of the earth's surface with a reasonably high geometric resolution [3]. In order to satisfy the increasing demand for large-scale scene imaging, attention has been turned to various acquisition modes of the SAR system.

The scanning SAR (ScanSAR) mode has been developed to promote the wide-swath imaging capability of the conventional stripmap SAR system, which slices the entire azimuth antenna pattern (AAP) to cover multiple swathes in the range dimension [4]. However, this mode has several drawbacks, such as a variation of the signal-to-noise ratio and the azimuth ambiguity ratio, and the scalloping phenomenon along azimuth [5]. Terrain observation by progressive scans (TOPS) [6] is an alternative that achieves the same capability as the ScanSAR but dramatically alleviates its drawbacks. The TOPS mode also employs a periodic stepwise beam switching to image several subswaths, which can be stitched together to form a wide-swath image. In azimuth, the beam is uniformly steered from aft to fore to generate a virtual shrinking of the AAP, entailing a complete illumination of each target in the scene. The experimental TOPS mode has been successfully implemented in the X-band TerraSAR-X [5] and the C-band RADARSAT-2 [7]. The European Space Agency's Sentinel-1A satellite has also employed the TOPS mode as its main operational mode, i.e., the interferometric wide-swath mode [8]. However, both the burst modes regretfully suffer a degradation of spatial resolution in the pursuit of wide-swath imaging, restricted by the minimum antenna area constraint inherent to a monoaperture system [3].

In recent years, detailed investigations on multichannel in azimuth SAR have revealed that the aforementioned contradiction can be effectively alleviated by collecting additional spatial samples for each transmitted pulse [9]. The effectiveness of the multichannel SAR system operating in the stripmap mode, including system design and signal processing, has been verified using German Aerospace Center's (DLA) F-SAR [10] and TerraSAR-X [11]. Besides, some RADATSAT-2 modes have been designed to use dual-channel receiver apertures to double the effective pulse repetition frequency (PRF) without sacrificing the swath width [12]. However, the continuous coherent monitoring of the earth with a weekly revisit time requires an imaging swath width of at least 400 km [13], which exceeds the capability of the conventional multichannel stripmap SAR with acceptable antenna dimensions. A possible solution to avoid an undue increase of the antenna length is the multichannel SAR system employing the burst mode operation [3]. Considering its superior performance, the TOPS acquisition mode in combination with the multichannel configuration is a promising candidate to achieve ultrawide-swath imaging with a reasonably high spatial resolution.

However, the new system concept for ultrawide imaging also faces many challenges. In addition to the complex system architecture of multiple subapertures configured with the 2-D beam sweeping, the signal processing of the multichannel TOPS SAR also necessitates novel solutions. In the multichannel TOPS mode, the beam rotation in the along-track direction within the data acquisition interval makes the Doppler bandwidth spanning more than N·PRF [13], which results in a more intricate Doppler aliasing. Consequently, the conventional spectrum reconstruction algorithms [14], [15], in their original form, cannot be applied directly. In order to address this problem, an innovative adaptively squinted multichannel processing strategy based on time-dependent blockwise division has been proposed in [3]. Inspired by the two-step focusing technique presented in [16] and [17], a kind of full-aperture strategy has been proposed [13], [18], which embeds the traditional multichannel reconstruction algorithm in the prefiltering step of the two-step procedure. Additionally, another full-aperture processing approach for the beam steering (BS) SAR has been presented in [19] and validated using the synthesized multichannel TOPS data originally obtained from a monoaperture airborne SAR. Although detailed theoretical analysis and innovative processing strategies have been provided for the signal reconstruction in the multichannel TOPS mode, to the best of our knowledge, these achievements have not been validated with real field-collected data. Moreover, another important aspect of real multichannel TOPS data processing—channel mismatch calibration—has also not been investigated in the literature.

Generally, considering the flexibility and cost, airborne SAR systems have always been a step ahead in terms of technical development, allowing demonstration of new techniques that are later implemented in spaceborne SAR missions [20]. As an operation verification method, experiments implemented with SAR systems mounted on an airborne platform can offer an opportunity to predict potential technical difficulties and provide valuable advices for future space-based SAR systems. Accordingly, a C-band airborne dual-channel TOPS SAR system was designed, and an experimental campaign was successfully carried out in late September 2014. This paper presents an introduction to this newly developed airborne SAR sensor and demonstrates the processing results using the experimental data obtained.

During the processing of the experimental data, we have also studied the problem of antenna phase center fluctuation (APCF) in the dual-channel TOPS SAR system. When the antenna beam rotates in azimuth, the subaperture antenna phase centers (APC) will no longer be along a straight line but swing periodically with the variant beam angle. The phenomenon of APCF introduces an unfavorable phase error, which should be compensated before signal reconstruction and subsequent image processing. In this study, we address this problem using two different methods: by calculating the phase error caused by APCF based on the data collection geometry, or by estimating and compensating the APCF-induced phase based on the echo signal.

This paper is organized as follows. Section II introduces the system specifics of the C-band airborne dual-channel TOPS SAR sensor. Section III describes the phenomenon of APCF
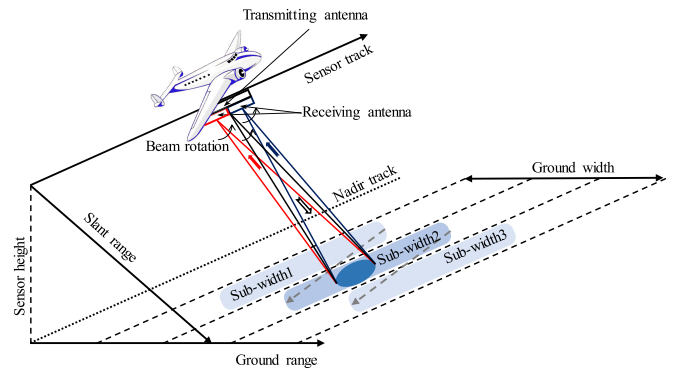

Fig. 1.   Imaging geometry of the airborne dual-channel TOPS mode.

in the dual-channel TOPS operation, and two kinds of calibration methods are developed to eliminate its influence. Subsequently, experimental dual-channel TOPS data processing, including channel mismatch calibration, unambiguous signal reconstruction, and subsequent single-channel TOPS data processing, is discussed in Section IV. The imaging results are presented and analyzed in Section V. Finally, in Section VI, this paper closes with a discussion and summary of our work.

II. Airborne Dual-Channel TOPS SAR System

The newly designed airborne SAR system on active service in the Institute of Electronics, Chinese Academy of Sciences, is mounted on a fixed-wing aircraft, which can fly over 8000 m above the ground with a mean velocity of approximately 130 m/s. In this experiment, the system was operated in the right-looking geometry, and a transmitting bandwidth of 200 MHz was selected to achieve a theoretical resolution of 0.75 m in the slant range dimension.

Equipped with a phased-array antenna (capable of scanning in both the azimuth and range directions), the versatile airborne SAR system can be commanded to work in various modes, including sliding spotlight, TOPS, and ScanSAR under azimuth dual-channel operating circumstances. When operated in the dual-channel TOPS mode, as shown in Fig. 1, the entire antenna (azimuth size of 0.624 m) was used to emit pulse waveform at the transmitting end (Tx) and was divided into two channels (0.312 m apart in azimuth) to receive the echoed signal in the receiving end (Rx). This transmitting–receiving antenna design guarantees a high transmission power and entails a hybrid AAP close to the pattern formed with the full antenna aperture in this system. In the cross-track dimension, three beams are arranged with a preset off-nadir angle of 44° (beam 1), 54° (beam 2), and 64° (beam 3), respectively. In the along-track dimension, both azimuth subapertures follow the same BS law to rotate uniformly from aft to fore within a span of 7.6° (beam 1), 7.0° (beam 2), and 6.2° (beam 3), respectively. The main configuration parameters of the airborne dual-channel TOPS SAR system are summarized in Table I.

It is necessary to illustrate that this airborne SAR system can be commanded to work with a fixed PRF or constant PRF-to-velocity ratio. In order to achieve equally spaced sampling

This article has been accepted for inclusion in a future issue of this journal. Content is final as presented, with the exception of pagination.

FAN *et al.*: DEMONSTRATION OF DUAL-CHANNEL TOPS SAR IMAGING WITH AIRBORNE C-BAND DATA

3

TABLE I
SAR SYSTEM PARAMETERS

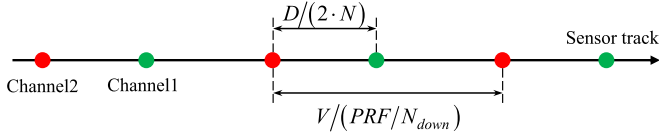| Parameters	Value		
Platform height	8600 m		
Carrier frequency	5.4 GHz		
Bandwidth	200 MHz		
Sampling rate	266 MHz		
PRF	1245 Hz		
Platform velocity	130 m/s		
Off-nadir-angle	44°	54°	64°
sweeping angle	±3.8°	±3.5°	±3.1°
Burst duration	1.36 s	1.54 s	1.82 s
Beam rotation rate	5.59°/s	4.55°/s	3.41°/s

Fig. 2. Azimuth spatial sampling of the dual-channel SAR system.

instead of equally temporal sampling, the PRF of the system can be instantaneously adjusted with the platform velocity. In the dual-channel TOPS experiment, the PRF of the system has been set to trace the platform velocity with a ratio of 9.6, i.e., $\mathrm{PRF}/V = 9.6 \text{ m}^{-1}$, where V signifies the sensor velocity.

In addition, since the data take obtained from the airborne SAR system exhibits high oversampling in azimuth, a preliminary decimation process has been performed to produce data takes of aliased channels. Different decimating strategies result in different azimuth signal sampling uniformities. As depicted in Fig. 2, the signal spatial uniformity can be calculated as follows:

$$\alpha = \frac{V/\left(\mathrm{PRF}/N_{\mathrm{down}}\right) - (N-1)\cdot D/\left(2\cdot N\right)}{D/\left(2\cdot N\right)} \quad (1)$$

where D is the azimuth antenna length, N stands for the channel number, and the original data is downsampled with N_{down}. According to (1), where 100% corresponds to the optimum offset with uniform sampling and 0% corresponds to coinciding samples [14], the sampling uniformity is 99.7% (three-to-one) and 33.5% (two-to-one), respectively.

III. APCF IN THE DUAL-CHANNEL TOPS MODE

The location of the radar is defined as the reference position from which radar measures range. In SAR systems, the APC is assumed to be the location where the antenna transmits and receives phase-encoded signals. The ability of a SAR system to create a high-resolution image is dependent on maintaining subwavelength knowledge of the platform position, i.e., the APC location, from pulse to pulse during the synthetic aperture time. Besides, in multichannel SAR systems, the success of nonuniform sampling reconstruction also relies on the accurate knowledge of the phase center locations.
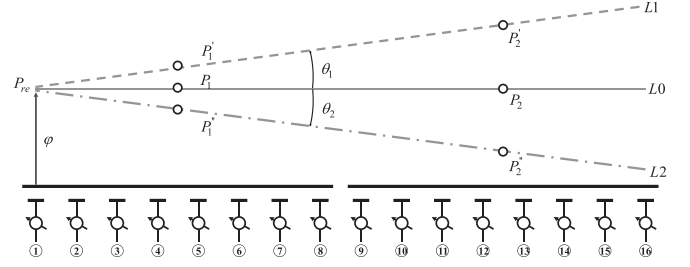

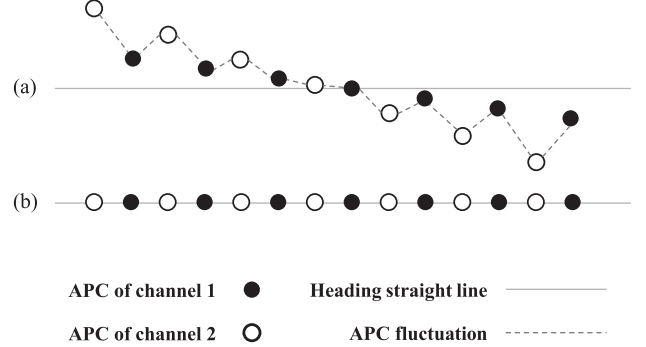Fig. 3. Phenomenon of APCF in the dual-channel TOPS system.

Fig. 4. APC of both channels during system operation. (a) Before and (b) after APCF calibration.

A. Phenomenon of APCF in the Dual-Channel TOPS Mode

In recent years, the phased-array antenna, which can change the beam direction in a flexible and reliable manner, has been widely utilized throughout the SAR community. In contrast to the mechanically rotating antenna, the effective AAP of the phased-array antenna is reinforced in the desired direction and suppressed in the undesired directions by introducing a relative phase offset in each array element. The phased-array antenna used in the airborne dual-channel TOPS system is composed of 4×16 (range × azimuth) array elements, each connected to a phase shifter. In this experiment, the outermost phase shifter (labeled ① in Fig. 3) is set as the reference phase point, where the applied offset phase is fixed during system operation. Other phase shifters work in variant states to achieve the rotation of the constant-phase wavefront. In Fig. 3, the dashed line $L1$ and the dotted-dashed line $L2$ stand for the electromagnetic constant-phase wavefront corresponding to beam rotation angle θ_1 and θ_2, respectively, and the solid line $L0$ signifies the constant-phase wavefront of the stripmap operation. Therefore, when the beam is steered in azimuth, the subaperture APCs will deviate accordingly from their expected positions (P_1 and P_2) and fluctuate by following a regular law. This phenomenon is referred to as APCF in the following sections.

In the dual-channel TOPS SAR system, the synthetical spatial samples originating from different channels produce a sawtooth-shaped appearance with time-variant beam pointing, as illustrated in Fig. 4(a). The resulting high-frequency phase error causes paired echoes in the system impulse response, which further results in unfavorable ambiguities in the imagery [21].

This article has been accepted for inclusion in a future issue of this journal. Content is final as presented, with the exception of pagination.

4   IEEE JOURNAL OF SELECTED TOPICS IN APPLIED EARTH OBSERVATIONS AND REMOTE SENSING
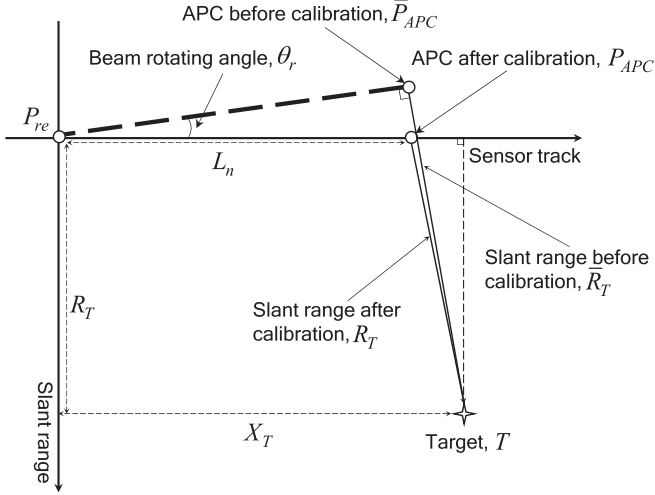

Fig. 5.   APCF sketched in the slant-range Cartesian coordinate system.

As derived in [21], the system performance of peak sidelobe level ratio (PSLR) is related to the amplitude of the sinusoid-like phase error Φ_0 as follows:

$$\text{PSLR} = \frac{\Phi_0^2}{4}. \tag{2}$$

Considering our C-band airborne dual-channel TOPS SAR system as an example, the beam rotates uniformly at an average rate of 0.0594 rad/s (beam 3) in azimuth within the angle span $[-3.1°, 3.1°]$. Typically, the zero-to-peak amplitude Φ_0 should be maintained within 0.35 rad to obtain a good PSLR(≤ -15 dB) [21], while the phase error between the two channels reaches as high as approximately 1.91 rad in the dual-channel TOPS system, i.e., at the start and end of a burst, which is beyond the tolerance of coherent azimuth processing. Consequently, some technical preprocessing is necessary to calibrate the fluctuating APCs to an ideal straight line in the heading direction, as presented in Fig. 4(b), before subsequent signal reconstruction.

It should be emphasized that the appearance of APCF is dependent on the selection of the reference phase center employed in this airborne SAR system. If each receiving channel is set with a reference phase point positioned at the center of each subaperture, theoretically, the phenomenon of APCF can be avoided. Otherwise, additional ground processing is necessary to cancel the influence of APCF.

B. APCF Calibration With the Data Acquisition Geometry

Subsequently, we provide further analysis of the fluctuating regularity of the APC in the dual-channel TOPS operation, and attempt to provide an analytical expression for direct APCF calibration. For the sake of mathematical tractability, a 2-D Cartesian coordinate system, illustrated in Fig. 5, is employed, which supports the slant range plane. It is assumed that the coordinates of the subaperture APC before and after calibration, i.e., $\overline{P}_{\text{APC}}$ and P_{APC}, and a scene target T are listed

as follows:

$$\begin{cases} T : (X_T, R_T) \\ P_{\text{APC}} : (L_n, 0) \\ \overline{P}_{\text{APC}} : (L_n, -L_n \cdot \tan(\theta_r)). \end{cases} \tag{3}$$

where $\theta_r = \omega t$ signifies the beam scanning angle, ω is the beam rotation rate, and t denotes the azimuth slow time. Furthermore, X_T and R_T describe the azimuth and slant-range position of target T, and L_n represents the physical along-track distance between the reference phase point and the APC of channel n. The phase history variation caused by APCF of the channel n can be calculated as follows:

$$\begin{aligned} \varphi_n &= \frac{2\pi}{\lambda}(\overline{R}_T - R_T) \\ &= \frac{2\pi}{\lambda}\sqrt{(X_T - L_n)^2 + (R_T + L_n \cdot \tan(\theta_r))^2} \\ &\quad - \frac{2\pi}{\lambda}\sqrt{(X_T - L_n)^2 + R_T{}^2}. \end{aligned} \tag{4}$$

Considering that the beam is steered within a small angle span (which is even smaller in the spaceborne situation), the hypothesis of (5) is satisfied

$$(X_T - L_n)^2 + R_T{}^2 \gg 2R_T L_n \tan(\theta_r) + (L_n \cdot \tan(\theta_r))^2. \tag{5}$$

Similarly, the quadratic term $(L_n \cdot \tan(\theta_r))^2$ can be safely omitted. Furthermore, the phase error caused by APCF can be simplified by a quadratic approximation

$$\varphi_n \approx \frac{2\pi}{\lambda}\frac{R_T}{\sqrt{(X_T - L_n)^2 + R_T{}^2}} \cdot L_n \cdot \tan(\theta_r). \tag{6}$$

Furthermore, the following equation can be derived by considering the imaging geometry of the dual-channel TOPS mode:

$$\cos(\theta_r) \approx \frac{R_T}{\sqrt{(X_T - L_n)^2 + R_T{}^2}}. \tag{7}$$

By inserting (7) into (6), the APCF phase error can be expressed as follows:

$$\varphi_n = \frac{2\pi}{\lambda} \cdot L_n \cdot \sin(\theta_r) \approx \frac{2\pi}{\lambda}L_n \omega t. \tag{8}$$

Assuming a small scanning angle and a uniform beam rotating velocity, the phase history error caused by APCF follows an approximately linear trend. Given the theoretical expression of (8), the APCF-induced phase mismatch can be effectively compensated in the azimuth time domain with the explicit system parameters λ, ω, and L_n.

C. APCF Calibration Based on Echo Data

The APCF calibration method proposed in Section III-B is derived from the data collection geometry, which is attractive from the computational perspective. Nevertheless, other factors, such as inaccurate measurements of the subaperture along-track distances [22] or inaccurate knowledge of the beam pointing

TABLE II
PROCEDURE OF APCF CALIBRATION BASED ON ECHOED DATA

APCF calibration procedure
Step 1   Perform range compression and range cell migration correction (RCMC) on the echo data of the reference channel.
Step 2   Azimuth multiplication of the range compressed data by the reference quadratic phase signal (9).
Step 3   Select these range bins with high energy, with the assumption that these range bins are more likely to encompass bright point-like scatterers.
Step 4   Perform fast Fourier transformation (FFT) in azimuth to obtain complex image.
Step 5   Perform a second selection to choose the range bins with isolated point-like scatterers using the contrast analysis method. Clip the section that includes the point scatterer with a proper window function in each range bin, whose width should approximately cover the energy distribution of the scatterer.
Step 6   Shift the selected scatterer to the azimuth center of each range bin to remove the position-relevant frequency offset. This is conducted by complex multiplication with a linear phase in the phase-history domain.
Step 7   Sum all the range bins in the cross-track dimension and find the phase history of the composite point-like target.
Step 8   Repeat the same process in the other channel, but with the same circular shift volume used in the reference channel in Step 6.
Step 9   After both channels finish the whole procedure, find the phase history difference between the two channels to give a maximum likelihood estimation of the APCF-induced phase mismatch.

[12], directly influence the calibrating performance. Accordingly, a model-independent method is developed in this section to eliminate the influence of APCF.

If there exists a high-intensity point-like scatterer in the illuminated scene, an analysis of the target phase history in different channels provides an estimation of the subaperture APC footmark. However, choosing a range bin with only one isolated high-intensity point-like scatterer in real data processing is unrealistic. In this study, we adopt the strategy of multipoint accumulation, with the hypothesis that the signal is superimposed coherently whereas noise is superimposed randomly. Moreover, the window functions are applied to preserve the width of the dominant energy distribution of each point target while discarding the part that cannot contribute to the processing.

However, the direct superimposition of the selected high-intensity scatterers in the range-compressed phase-history domain is problematic, since they possess different Doppler frequency offsets and different original phases [23]. Coherent superimposition of multiple signals demands that their Doppler history and original phase should be consistent. In order to address this problem, two elegant processing strategies have been employed, which are inspired by the phase gradient autofocus technique [23]. First, the strongest scatterer in each range bin is selected and shifted to the azimuth center to remove the frequency offset. Subsequently, in order to resolve the conflict arising from inconsistent original phase, the difference between the phase history estimation of different channels is determined. The complete procedure of APCF phase estimation is summarized in Table II. The selected reference signal used in Step 2 is given as follows:

$$h_{1,n}(t) = \exp\left[j\pi \frac{2V^2}{\lambda \tilde{r}} \cdot \left(t - \frac{\Delta x_n}{2V}\right)^2\right]. \qquad (9)$$

where $\tilde{r}$ represents the slant range array and Δx_n is the physical along-track distance between the transmitting antenna and the nth receiving antenna.

D. Verification With Simulated Data

An airborne scene with multiple point scatterers is simulated to validate the newly developed APCF calibration methods, and the main system parameters are set according to our airborne
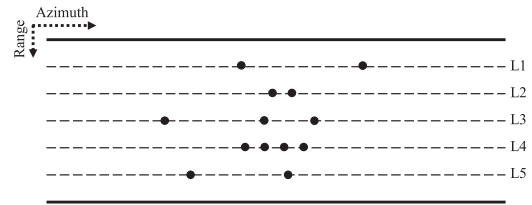

Fig. 6. Designed experimental scene with multiple point-like scatterers.

SAR system. The distribution of the simulated point scatterers is illustrated in Fig. 6, where the points are set to be relatively random. In addition, these targets are weighted with different intensities to represent distinguishable reflecting radar cross sections. The APCF phase calculation method proposed in Section III-B is scene insensitive and can be implemented directly with (8). The APCF phase error obtained is compared to the data-based APCF calibration output in the following section.

The simulated data are subsequently input into the data processor designed using Table II. Since the operations of range compression, RCMC, and azimuth dechirp have been sufficiently investigated in a previous study [24], they are not discussed in detail in this paper. Subsequently, we proceed to choose range bins that contain isolated high-intensity point-like scatterers. In practical implementations, the energy-based criterion can screen out the range bins, which stand a good chance of including high-intensity point-like scatterers, and the contrast-based selection allows us to effectively exclude those range bins that encompass more than one neighboring target. Subsequently, proper windows are applied to the selected high-power scatterers and the operation of circular shift is performed. Finally, the summation of all the selected range bins in the cross-track dimension entails a composite point target, and a phase history can be obtained. After all the channels are implemented with the data processor, the difference between the phase history of the reference channel and the other channel is considered as the final APCF phase error estimation.

Fig. 7(a) relates to the APCF phase error between the two channels obtained using the aforementioned calibration methods. It is evident that the calculated APCF phase (green) is consistent with the estimated APCF phase (blue), and an almost linear trend is easily observed.

This article has been accepted for inclusion in a future issue of this journal. Content is final as presented, with the exception of pagination.

6   IEEE JOURNAL OF SELECTED TOPICS IN APPLIED EARTH OBSERVATIONS AND REMOTE SENSING
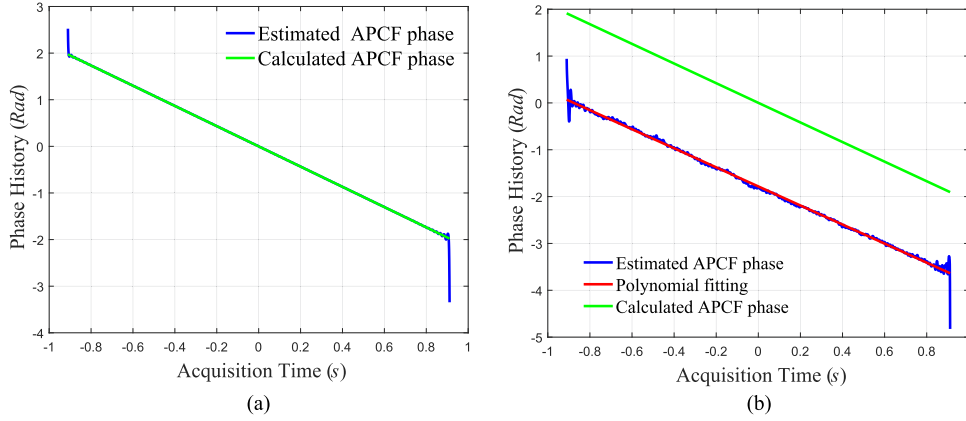

Fig. 7. APCF phase error extraction. (a) Simulated experiment: estimated APCF phase (blue) and calculated APCF phase (green). (b) Experiment with field-collected data: estimated APCF phase (blue) and its polynomial fitting result (red), calculated APCF phase with system parameters (green).

E. Verification With Real Dual-Channel TOPS Data

The same plots shown in Fig. 7(a) but with the airborne dual-channel TOPS experimental results are illustrated in Fig. 7(b). It is evident that a similarly linear trend of the APCF phase estimation (blue) can also be obtained. Besides, the calculated APCF phase (green) acquired using (8) is also presented, which is approximately parallel to the estimation based on the echoed data. It is worth noting that there is a fixed phase offset between the two APCF calibration outputs. This is reasonable since the data-driven method also has the potential to extract other systematic phase mismatches simultaneously. Accordingly, the data-based APCF calibration method can be classified as a kind of channel mismatch calibration technique.

In practical processing, the subaperture closer to the reference phase point is selected as the reference channel, and the APCF-induced phase extracted, as plotted in Fig. 7(b), is applied to the other channel to achieve consistent transfer functions. For better illustration of the performance, the interferometric phase diagrams between the two channels are presented in Figs. 10 and 11. It is evident that, after the APCF calibration, the approximately linear phase characteristic along azimuth in Figs. 10(a) and 11(a) has been effectively eliminated, as illustrated in Figs. 10(b) and 11(b). As discussed previously, other system phase mismatches can also be partially calibrated by the estimated APCF calibration method. This advantage results in a greener interferometric phase diagram, via the comparison of Fig. 11(b) with Fig. 10(b), indicating a closer phase characteristic between the two channels. The residual phase mismatch will be resolved in the following section of channel mismatch calibration.

IV. MULTICHANNEL PROCESSING

Compared with the ScanSAR operation, the signal acquired in the TOPS mode possesses different properties owing to the utilization of beam rotation in azimuth. In this section, subsequent processing of the airborne dual-channel TOPS data follows the flowchart shown in Fig. 8.
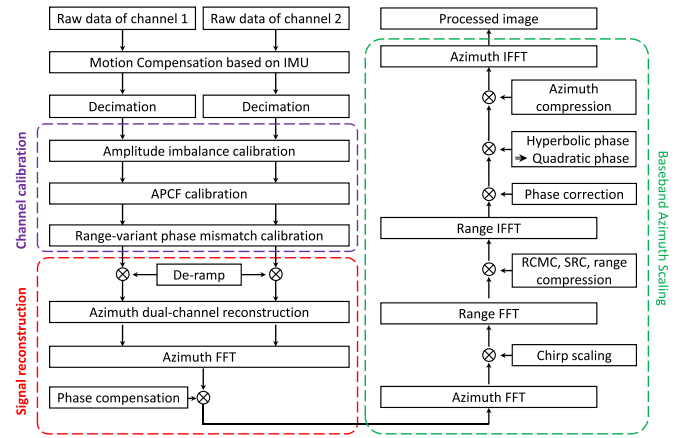

Fig. 8. Block diagram of the airborne dual-channel TOPS data processing.

A. Channel Mismatch Cancellation

Prior to the unambiguous reconstruction of the multichannel SAR signal, each channel needs to be well calibrated; otherwise, the performance of the reconstruction processor will degrade or even lose its effectiveness [25]. In practice, interferences in the returned signal among different channels are unavoidable. It could be due to, for instance, nonideal receiver hardware, antenna attitude, or different antenna gain patterns. Generally, the channel mismatches can be approximately classified into three categories: amplitude imbalance, range sampling time error, and phase mismatch. Usually, the amplitude imbalance results from inconsistent antenna patterns, which can be adaptively calibrated in the range-frequency domain [22] as follows:

$$\Delta A_m \left(f_r\right) = \frac{\int \left|S_1 \left(f_r, t\right)\right| dt}{\int \left|S_2 \left(f_r, t\right)\right| dt} \tag{10}$$

where $S_1(f_r, t)$ and $S_2(f_r, t)$ signify the dual-channel signal in the range-frequency domain. Fig. 9 presents the amplitude of the signal Doppler spectra before and after calibration. The influence of the range sampling time error, mainly caused by the differences between the analog-to-digital devices and a poor

This article has been accepted for inclusion in a future issue of this journal. Content is final as presented, with the exception of pagination.

FAN *et al.*: DEMONSTRATION OF DUAL-CHANNEL TOPS SAR IMAGING WITH AIRBORNE C-BAND DATA 7
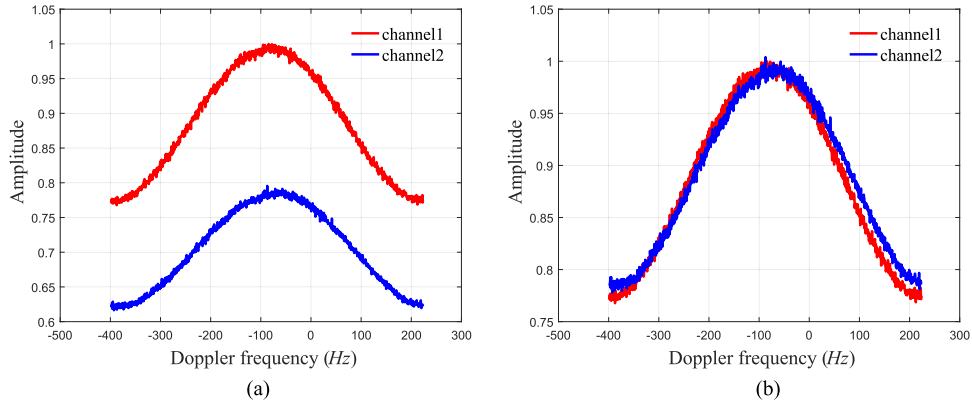

Fig. 9. Amplitude characteristic of the downsampled dual-channel signal. (a) Before calibration and (b) after calibration.
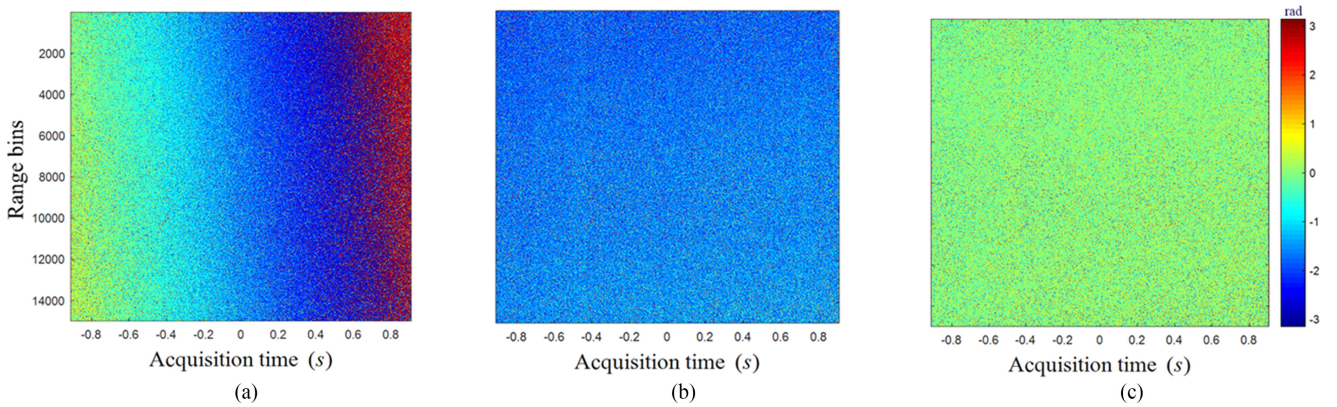

Fig. 10. Interferometric phase of the experimental data. (a) Before any calibration. (b) After calculated APCF calibration. (c) After residual phase compensation.
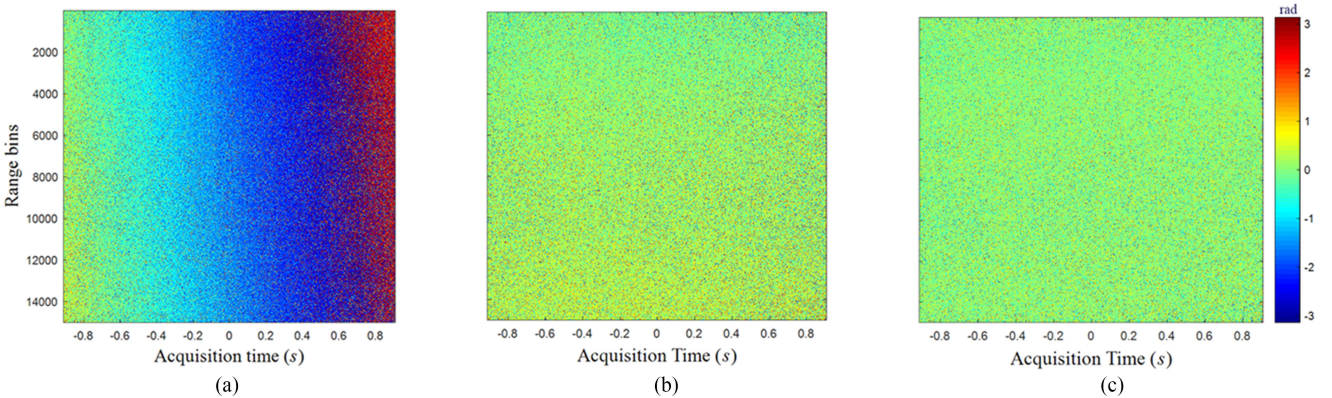

Fig. 11. Interferometric phase of the experimental data. (a) Before any calibration. (b) After estimated APCF calibration. (c) After residual phase compensation.

performance of the synchronizing circuit, can be effectively compensated by the internal calibration system.

Practically, phase mismatch dominates the ambiguous response in the reconstructed imagery [10]. In the airborne situations, owing to the impact of crosswind and airflow, the antenna baseline usually deviates from the ideal sensor track. As derived in [26], the perpendicular baseline, mainly caused by the antenna yaw and pitch, results in range-variant phase mismatches. In the case of this airborne SAR system, a yaw of $1°$ causes a phase mismatch of approximately $32°$ and a pitch of $1°$

causes a phase mismatch of approximately $15°$. Besides, other factors such as receiver hardware differences result in additional approximately constant phase mismatch. Various methods have been introduced in the literature for the calibration of phase mismatch [25]–[28]. In this study, we choose to employ the azimuth cross correlation method [28] to address the residual phase mismatch. In practical processing, the echoed signal is divided into blocks in the cross-track dimension to calibrate the range-variant phase mismatch. The entire greenish appearance of the interferometric phase diagram, as shown in Figs. 10(c)
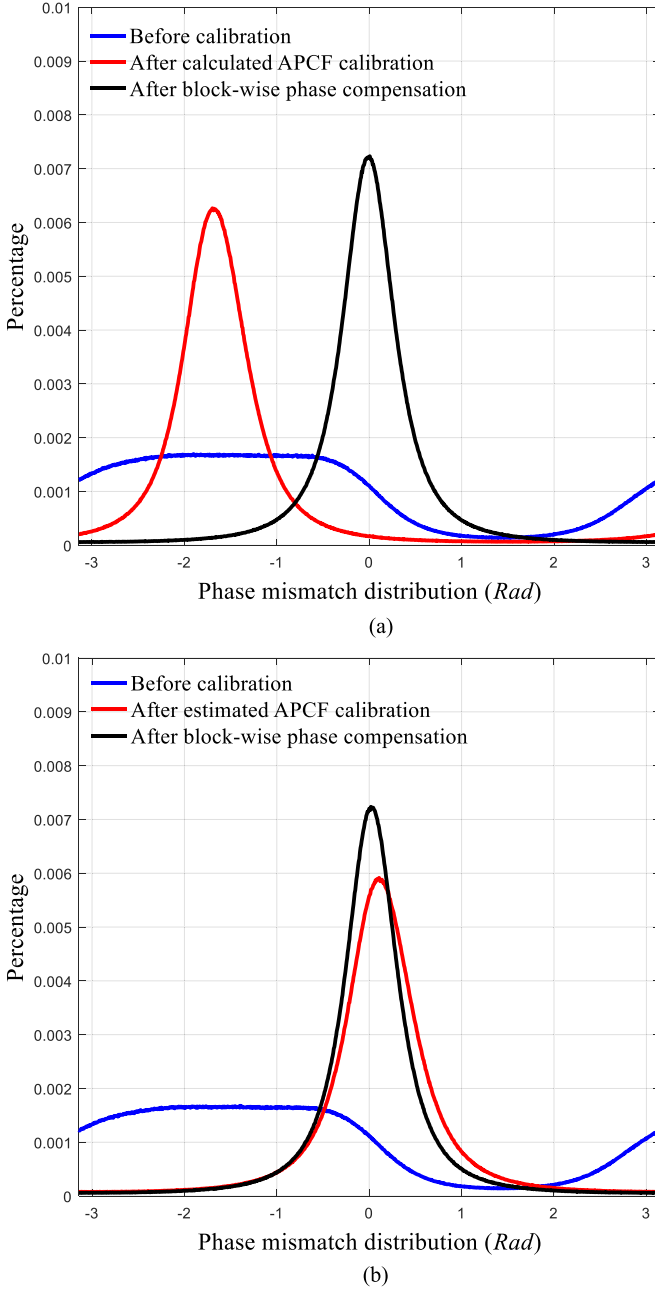
Fig. 12.   Distribution of interferometric phase between two channels with (a) the calculated APCF calibration and (b) the estimated APCF calibration.

and 11(c), indicates that the channel interferometric phase distribution is now centered round 0 rad.

In order to provide an intuitive demonstration and comparison, an analysis of the phase statistic histogram is performed, which is presented in Fig. 12. The plotted curves reveal the interferometric phase distribution of Figs. 10 and 11, respectively. Without calibration, the phase mismatch distribution spreads dispersively (blue), owing to the influence of APCF and channel phase mismatch. After calibrating the phase error caused by APCF, the phase distribution appears more concentrated, but with the peak deviated from 0 rad (red). After the blockwise cal-

ibration of phase mismatch, the sharp-shaped and zero-centered phase distribution (black) is aligned with the result shown in Figs. 10(c) and 11(c), which illustrates the effectiveness of channel mismatch calibration.

B. Nonuniform Sampling Reconstruction

With multiple azimuth receiving subapertures, the multichannel high-resolution wide-swath (HRWS) SAR systems resolve azimuth temporal subsampling using additional spatial samples. Besides, a suitable reconstruction processor is required to deal with the nonuniformly sampled multichannel data. In the multichannel TOPS mode, azimuth beam progressive sweeping results in a broaden Doppler bandwidth; hence, the conventional reconstruction algorithms [14], [15] cannot be applied directly in their original forms. In order to address this problem, various processing methods have been proposed in the literature [3], [13], [18], [19]. In our work, the preprocessing strategy proposed in [13] has been applied to achieve unambiguous reconstruction of the dual-channel TOPS data, which combines the two-step focusing technique in [16] with the conventional multiple reconstruction filter processing [14].

Similar to the Spectral Analysis algorithm [24], the key point of the prefiltering is the azimuth convolution of the raw data by the quadratic phase signal $h_{2,n}(t)$:

$$h_{2,n}(t) = \exp\left[j\pi \frac{2V^2}{\lambda R_{\text{rot}}} \cdot \left(t - \frac{\Delta x_n}{2V} \right)^2 \right] \qquad (11)$$

where $R_{\text{rot}} = -V_g/\omega$ and V_g is the ground beam velocity. Further calculation shows that the operation of azimuth convolution can be implemented with a chirp multiplication, a subsequent Fourier transform (FT), and a residual phase compensation [13]. An azimuth multichannel reconstruction algorithm can subsequently be embedded in the prefiltering step to achieve the unambiguous recovery of the Doppler spectrum.

Fig. 13 presents the reconstructed Doppler spectra using different resampling of the original data. Generally, unambiguous Doppler spectra in both situations have been recovered. A further inspection of Fig. 13(a) reveals a discontinuity, which is almost invisible in 13(b). Similar results also occurred when processing the TerraSAR-X experimental data in the dual receiver antenna mode [11], which is reasonable since the channel mismatch compensation is never perfect. In the dual-channel data reconstruction, the Doppler spectrum is separately recovered within the range of $[-\text{PRF}, f_{\text{dc}}]$ and $[f_{\text{dc}}, \text{PRF}]$, which are subsequently concatenated to produce a wide Doppler spectrum. The Doppler spectrum amplitude of the reconstruction filter function shows a staircase-like behavior, which is relevant with the signal sampling uniformity. The residual imbalance will cause an inaccurate reconstruction, which makes the Doppler spectrum interrupted at the conjunction of the reconstruction filter, and the jump in the reconstructed spectrum is related to the sampling uniformity.
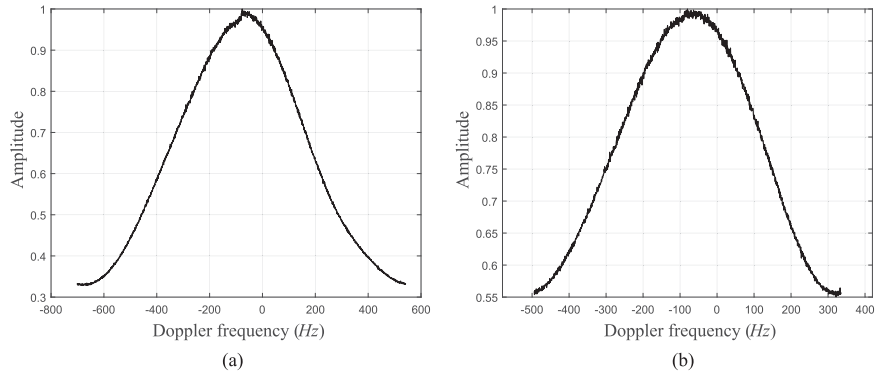
This article has been accepted for inclusion in a future issue of this journal. Content is final as presented, with the exception of pagination.

FAN *et al.*: DEMONSTRATION OF DUAL-CHANNEL TOPS SAR IMAGING WITH AIRBORNE C-BAND DATA 9

(a)

(b)

Fig. 13. Reconstructed Doppler spectrum with different preliminary decimation processes: (a) two-to-one and (b) three-to-one.
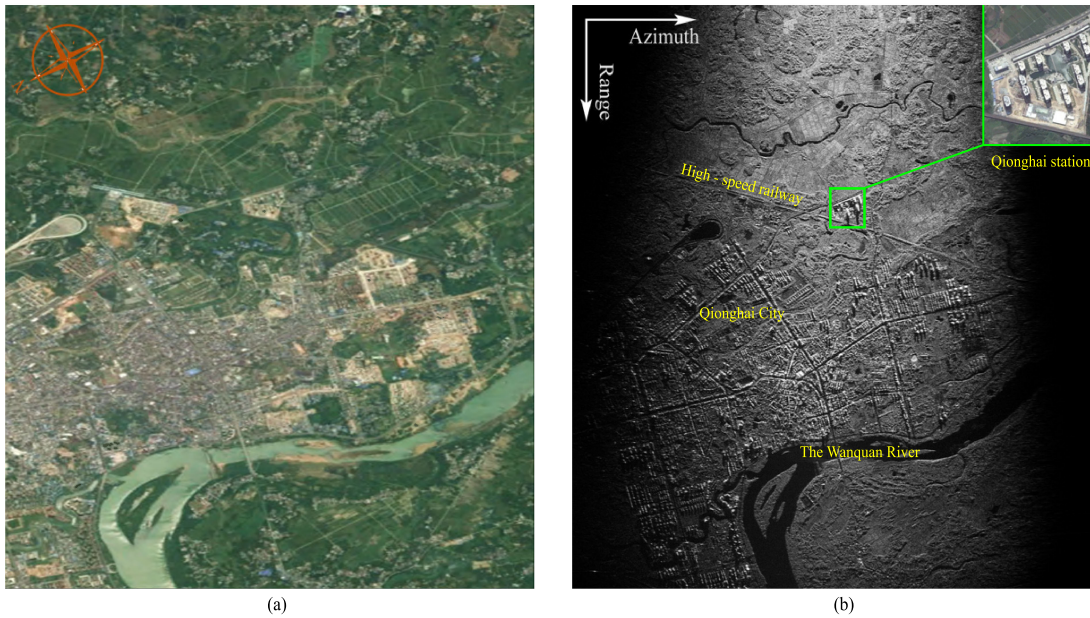

(a)

(b)

Fig. 14. Experimental scene. (a) Optical image (Copyright Google). (b) Reference image obtained with oversampled single-channel data.
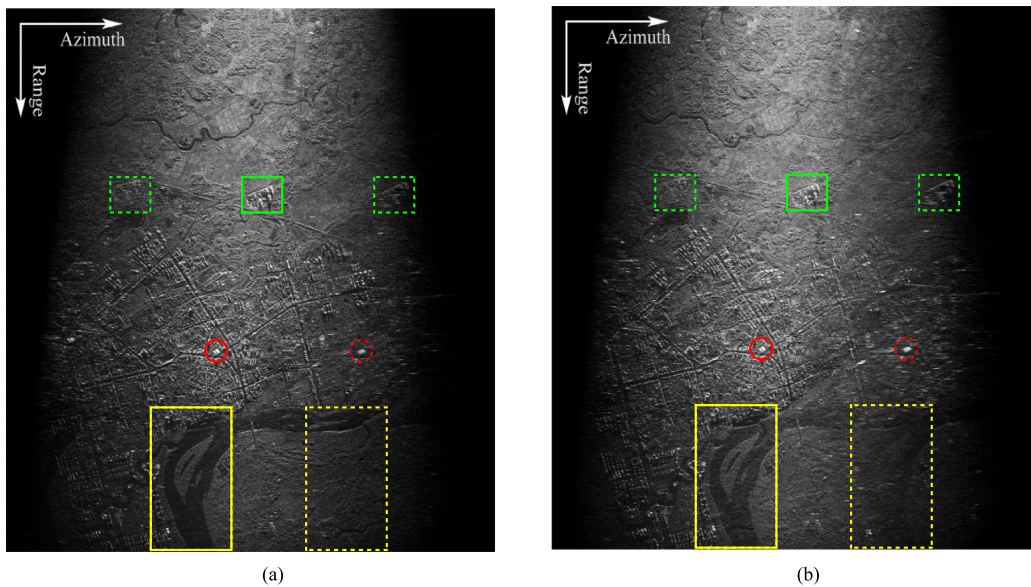

(a)

(b)

Fig. 15. Ambiguous imaging results with incomplete process of channel mismatch cancellation. (a) Image processed without channel mismatch calibration. (b) Image processed with conventional channel mismatch calibration. The real targets are circled with solid-line polygons and the ambiguities are circled with dashed-line polygons.
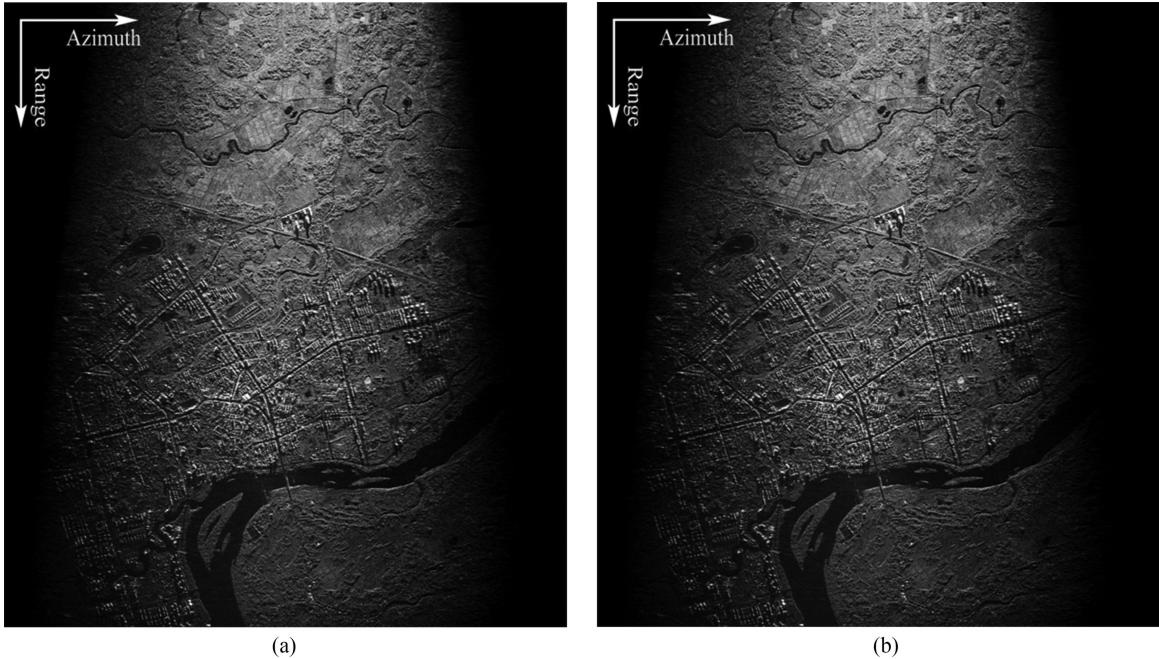
This article has been accepted for inclusion in a future issue of this journal. Content is final as presented, with the exception of pagination.

10   IEEE JOURNAL OF SELECTED TOPICS IN APPLIED EARTH OBSERVATIONS AND REMOTE SENSING

Fig. 16.   Reconstructed imageries with (a) the calibrated APCF calibration and (b) the estimated APCF calibration.

C. Processing of Coherent Single-Channel TOPS Data

After the unambiguous reconstruction, the acquired data can be regarded as that sampled by an equivalent single-channel TOPS system. Many studies have contributed to the processing of monoaperture TOPS data [29]–[31]. The baseband azimuth scaling approach proposed in [32] has been employed in our work to process the reconstructed single-channel TOPS data. The key aspect of the procedure is the replacement of the hyperbolic azimuth phase with a purely quadratic phase function before azimuth compression [32], which successfully addresses the azimuth folding of the focused image.

V. IMAGING RESULTS

The dataset processed in this study was acquired during an experimental campaign conducted on the eastern shore of Hainan Province in late September 2014. Fig. 14 presents the ambiguity-free image processed with oversampled single-channel data, along with an optical reference image from Google Earth. It is evident that, owing to the utilization of azimuth beam rotation from aft to fore, the TOPS image shows wider coverage in the far range than in the near range. The illuminated scene shows the urban area of Qionghai City, which is located near the Wanquan River. This image is obtained from an azimuth burst of beam 3 (with off-nadir angle $64°$) with azimuth one-look processing. The vertical side corresponds to the range direction, from (top) near to (bottom) far. The slant range swath is approximately 7.9 km and the azimuth extension is approximately 5.1 km.

Fig. 15(a) presents the ambiguous image reconstructed using the dual-channel TOPS experimental data, but without calibrating the channel mismatches of the multichannel SAR system. Compared with the reference image of Fig. 14(b), the noteworthy features in Fig. 15(a) are the following. First, the entire image is heavily blurred, and the reduction of image readability
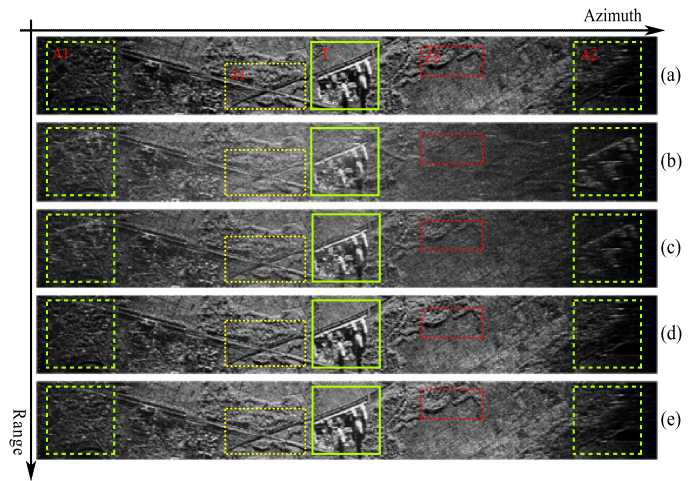

Fig. 17.   Partial enlargements of the Qionghai Railway Station in obtained SAR images. (a) is obtained from Fig. 14(b). (b) and (c) are obtained from Fig. 15(a) and (b). (d) and (e) are obtained from Fig. 16(a) and (b).

caused by untreated channel mismatches is significant. Second, the ambiguities associated with the Wanquan River and the Qionghai high-speed railway station appear significantly. Finally, the weak-scattering Wanquan River at the lower part of the image is significantly polluted by the ambiguities of the contextual surroundings. In Fig. 15(b), the image processed with the conventional channel mismatch calibration is illustrated. In this processing, the channel amplitude mismatch is calibrated using the procedure presented in Section IV, and the phase mismatch is addressed using the azimuth cross correlation method. The image quality has been improved to a certain extent, but the ambiguities of high-reflecting targets are still visible.

Fig. 16 exhibits the images obtained using the process shown in the flowchart of Fig. 8, including the channel amplitude
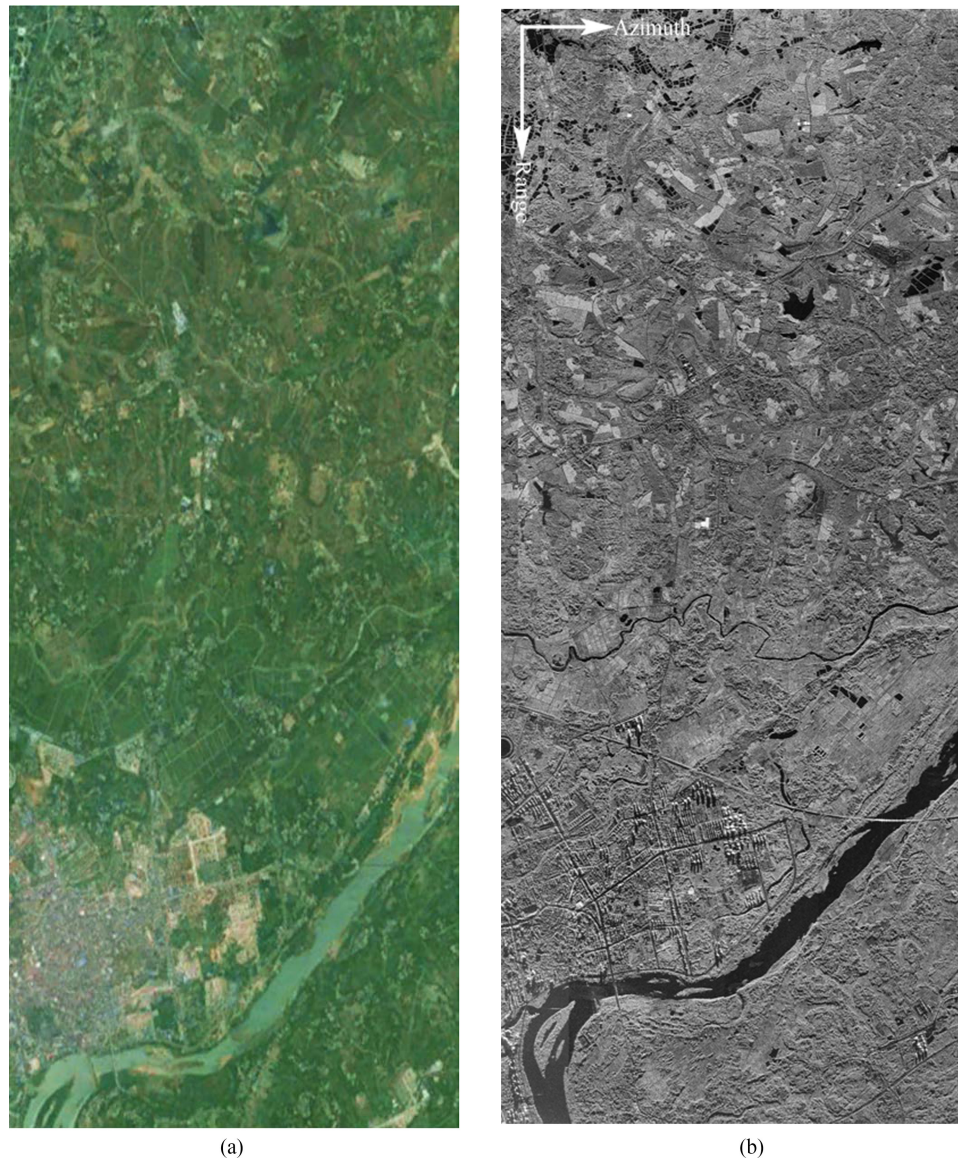
Fig. 18. Mosaic imagery formed with six bursts in azimuth and three beams in range. (a) Illuminated area presented in Google Earth (Copyright Google). (b) Stitched large-scale image in the azimuth dual-channel TOPS mode.

mismatch cancellation, APCF-induced phase mismatch calibration, residual phase mismatch compensation, and multichannel signal reconstruction. Both APCF phase calibrating methods proposed in Section III have been utilized. Fig. 16(a) shows the image processed using the calculated APCF processing, and Fig. 16(b) shows the image processed using the estimated APCF processing. It is evident that the imaging performances are highly improved and are visually close to the reference image.

Fig. 17 provides the corresponding zooms of the obtained SAR images of the Qionghai railway station for further comparison. Accordingly, Fig. 17(a) is from Fig. 14(b); 17(b) and (c) from Fig. 15(a) and (b), respectively; and 17(d) and (e) from Fig. 16(a) and (b), respectively. Noticeable effects of uncompensated channel mismatches can be observed in Fig. 17(b). First, the paired ambiguities of the high-scattering buildings in the area T appear symmetrically at the areas of A1 and A2 in Fig. 17(b). Second, compared with Fig. 17(a), the image con-

trast in the area T appears much more attenuated in Fig. 17(b). This is a direct consequence of the Doppler spectrum aliasing, which leaks energy of the real target to the ghost targets. A similar phenomenon can be observed in the areas Z1 and Z2. In Fig. 17(c), the situation is improved, but the ambiguities are still visible. With additional processing of the APCF calibration, as shown in Fig. 17(d) and (e), it is evident that the image contrast has been greatly improved and the ambiguities have been effectively suppressed.

In the TOPS operational mode, the bursts in both directions need to be connected together to achieve continuous wide-swath imaging. In this section, six bursts in azimuth and three beams in elevation are combined together to cover an area of about 7 km $\times$ 16 km (azimuth $\times$ range). Fig. 18 illustrates the sutured single-look TOPS SAR image and a corresponding optical image from Google Earth. A detailed inspection of both images reveals satisfactory connection of the illuminated scene, such as the

continuous rivers and urban streets. Besides, the absence of scalloping is evident.

VI. DISCUSSIONS AND CONCLUSION

A multichannel SAR system in the TOPS mode combines the advantages of both operations, i.e., the HRWS imaging capability of multichannel in azimuth technique and the extended coverage mapping capability of the TOPS mode; thus, it is a promising candidate for ultrawide-swath imaging applications. In this paper, a C-band dual-channel airborne SAR system in the TOPS operation was systematically introduced, as a test bed for future spaceborne realizations. With the field-collected experimental data, the complete data processing flow and the final imaging results were presented.

In addition, the phenomenon of APCF in this dual-channel TOPS SAR system was discussed, and two kinds of calibrating techniques were proposed to address the problem. With an accurate measurement of the subaperture along-track distance and a precise knowledge of the beam pointing, the calculated APCF calibration method is competent and computationally attractive. Otherwise, the estimated APCF calibration based on the echo data can be utilized to obtain robust performance, which is relatively time consuming.

It is worth mentioning that, despite being developed for the dual-channel TOPS SAR system, the processing flow will provide a useful reference for multichannel sliding spotlight SAR data processing, owing to the similar time–frequency relationship of both modes. Actually, we have performed another airborne experiment working in the azimuth dual-channel sliding spotlight mode, for the applications that prefer very high spatial resolution with wide-swath coverage, such as transportation infrastructure management in the urban environment. Efforts are being currently undertaken in our team to investigate this interesting SAR mode with the experimental data.

REFERENCES

[1] N. Gebert, G. Krieger, and A. Moreira, "High resolution wide swath SAR imaging with digital beamforming—Performance analysis, optimization, system design," in *Proc. Eur. Conf. Synthetic Aperture Radar*, Dresden, Germany, Jul. 2006, pp. 341–344.

[2] N. Gerbert, G. Krieger, and A. Moreira, "Digital beamforming on receive: Techniques and optimization strategies for HRWS SAR imaging," *IEEE Trans. Aerosp. Electron. Syst.*, vol. 45, no. 2, pp. 564–592, Apr. 2009.

[3] N. Gebert, G. Krieger, and A. Moreira, "Multichannel azimuth processing in ScanSAR and TOPS mode operation," *IEEE Trans. Geosci. Remote Sens.*, vol. 48, no. 7, pp. 2994–3008, Jul. 2010.

[4] R. K. Moore, J. P. Claassen, and Y. H. Lin, "Scanning spaceborne synthetic aperture radar with integrated radiometer," *IEEE Trans. Aerosp. Electron. Syst.*, vol. AES-17, no. 3, pp. 410–421, May 1981.

[5] A. Meta, J. Mittermayer, P. Prats, R. Scheiber, and U. Steinbrecher, "TOPS imaging with TerraSAR-X: Mode design and performance analysis," *IEEE Trans. Geosci. Remote Sens.*, vol. 48, no. 2, pp. 759–769, Feb. 2010.

[6] F. D. Zan and A. M. Guarnieri, "TOPS: Terrain observation by progressive scan," *IEEE Trans. Geosci. Remote Sens.*, vol. 44, no. 9, pp. 2352–2360, Sep. 2006.

[7] G. Davidson, V. Mantle, B. Rabus, D. Williams, and D. Geudtner, "Implementation of TOPS mode on RADARSAT-2 in support of the Sentinel-1mission," in *Proc. ESA Living Planet Symp.*, Edinburgh, U.K., Sep. 2013, p. 160.

[8] N. Yague-Martinez, P. Prats-Iraola, and F. R. Gonzalez, "Interferometric processing of Sentinel-1 TOPS data," *IEEE Trans. Geosci. Remote Sens.*, vol. 54, no. 4, pp. 2220–2234, Apr. 2016.

[9] N. Gebert, "Multichannel azimuth processing for high-resolution wide-swath SAR imaging," Ph.D. dissertation, German Aerosp. Center, Cologne, Germany, 2009.

[10] N. Gebert, F. de Almeida, and G. Krieger, "Airborne demonstration of multichannel SAR imaging," *IEEE Geosci. Remote Sens. Lett.*, vol. 8, no. 5, pp. 963–967, Sep. 2011.

[11] J. Kim, M. Younis, P. Pau, M. Gabele, and G. Krieger, "First spaceborne demonstration of digital beamforming for azimuth ambiguity suppression," *IEEE Trans. Geosci. Remote Sens.*, vol. 51, no. 1, pp. 579–590, Jan. 2013.

[12] D. Williams, P. LeDantec, and M. Chabot, "RADARSAT-2 image quality and calibration update," in *Proc. Eur. Conf. Synthetic Aperture Radar*, Berlin, Germany, Apr. 2014, pp. 1053–1056.

[13] W. Xu, P. Huang, R. Wang, and Y. Deng, "Processing of multichannel sliding spotlight and TOPS synthetic aperture radar data," *IEEE Trans. Geosci. Remote Sens.*, vol. 51, no. 8, pp. 4417–4429, Aug. 2013.

[14] G. Krieger, N. Gebert, and A. Moreira, "Unambiguous SAR signal reconstruction from nonuniform displaced phase center sampling," *IEEE Geosci. Remote Sens. Lett.*, vol. 1, no. 4, pp. 260–264, Oct. 2004.

[15] Z. Li, H. Wang, T. Su, and Z. Bao, "Generation of wide-swath and high-resolution SAR images from multichannel small spaceborne SAR system," *IEEE Geosci. Remote Sens. Lett.*, vol. 2, no. 1, pp. 82–86, Jan. 2005.

[16] R. Lanari, M. Tesauro, E. Sansosti, and G. Fornaro, "Spotlight SAR data focusing based on a two-step processing approach," *IEEE Trans. Geosci. Remote Sens.*, vol. 39, no. 9, pp. 1993–2004, Sep. 2001.

[17] R. Lanari, S. Zoffoli, E. Sansosti, G. Fornaro, and F. Serafino, "New approach for hybrid strip-map/spotlight SAR data focusing," *IEE Proc.—Radar, Sonar Navigat.*, vol. 148, pp. 363–372, Dec. 2001.

[18] P. Huang, S. Li, and W. Xu, "Investigation on full-aperture multichannel azimuth data processing in TOPS," *IEEE Geosci. Remote Sens. Lett.*, vol. 11, no. 4, pp. 728–732, Apr. 2014.

[19] G. Sun, M. Xing, and X. Xia, "Multichannel full-aperture azimuth processing for beam steering SAR," *IEEE Trans. Geosci. Remote Sens.*, vol. 51, no. 9, pp. 4761–4778, Sep. 2013.

[20] A. Moreira, P. Prats, and M. Younis, "A tutorial on synthetic aperture radar," *IEEE Geosci. Remote Sens. Mag.*, vol. 1, no. 1, pp. 4417–4429, Apr. 2013.

[21] V. C. Koo, T. S. Lim, and M. V. Rao, "A GA-based autofocus technique for correcting high-frequency SAR phase error," *J. Electromagn. Waves Appl.*, vol. 18, pp. 781–795, Aug. 2004.

[22] C. H. Gierull, "Digital channel balancing of along-track interferometric SAR data," DRDC Ottawa, Ottawa, ON, Canada, Tech. Memorandum 2003-024, Mar. 2003.

[23] D. E. Wahl, P. H. Eichel, D. C. Ghiglia, and C. V. Jakowatz, "Phase gradient autofocus—A robust tool for high resolution SAR phase correction," *IEEE Trans. Aerosp. Electron. Syst.*, vol. 30, no. 3, pp. 827–835, Jul. 1994.

[24] I. G. Cumming and F. H. Wong, *Digital Processing of Synthetic Aperture Radar Data: Algorithms and Implementation*. Norwood, MA, USA: Artech House, 2005.

[25] Z. Li, Z. Bao, H. Wang, and G. Liao, "Performance improvement for constellation SAR using signal processing techniques," *IEEE Trans. Aerosp. Electron. Syst.*, vol. 42, no. 2, pp. 436–452, Apr. 2006.

[26] S. Zhang, M. Xing, and X. Xia, "Multichannel HRWS SAR imaging based on range-variant channel calibration and multi-Doppler-direction restriction ambiguity suppression," *IEEE Trans. Geosci. Remote Sens.*, vol. 52, no. 7, pp. 4306–4327, Jul. 2014.

[27] L. Zhang, M. Xing, C. Qiu, and Z. Bao, "Adaptive two-step calibration for high resolution and wide-swath SAR imaging," *IET Radar Sonar Navigat.*, vol. 4, pp. 548–559, Aug. 2010.

[28] J. Feng, C. Gao, Y. Zhang, and R. Wang, "Phase mismatch calibration of the multichannel SAR based on azimuth cross correlation," *IEEE Geosci. Remote Sens. Lett.*, vol. 10, no. 4, pp. 903–907, Jul. 2013.

[29] W. Xu, P. Huang, R. Wang, Y. Deng, and Y. Lu, "TOPS-mode raw data processing using chirp scaling algorithm," *IEEE J. Sel. Topics Appl. Earth Observ.*, vol. 7, no. 1, pp. 235–246, Jan. 2014.

[30] W. Xu, P. Huang, Y. Deng, J. Sun, and X. Shang, "An efficient approach with scaling factors for TOPS-mode SAR data focusing," *IEEE Geosci. Remote Sens. Lett.*, vol. 8, no. 5, pp. 929–933, Sep. 2011.

[31] Y. Wu, G. Sun, X. Xia, M. Xing, J. Yang, and Z. Bao, "An azimuth frequency non-linear chirp scaling (FNCS) algorithm for TOPS SAR imaging with high squint angle," *IEEE J. Sel. Topics Appl. Earth Observ.*, vol. 7, no. 1, pp. 213–221, Jan. 2014.

[32] P. Prats, R. Scheiber, J. Mittermayer, A. Meta, and A. Moreira, "Processing of sliding spotlight and TOPS SAR data using baseband azimuth scaling," *IEEE Trans. Geosci. Remote Sens.*, vol. 48, no. 2, pp. 770–780, Feb. 2010.

Huaitao Fan received the B.S. degree in electronic information science and technology from Ocean University of China, Qingdao, China, in 2012. He is currently working toward the Ph.D. degree with the Department of Space Microwave Remote Sensing System, Institute of Electronics, Chinese Academy of Sciences, Beijing, China.

He is also with the University of Chinese Academy of Sciences, Beijing, China. His research interests include multichannel in azimuth synthetic aperture radar imaging.

Zhimin Zhang received the B.S. degree in electrical engineering from Beijing Institute of Technology, Beijing, China, in 1992, and the M.S. degree from the Graduate University of Chinese Academy of Sciences, Beijing, in 1995.

In 1995, he joined the Institute of Electronics, Chinese Academy of Sciences, Beijing, where he worked on radar system design and signal processing. His research interests include spaceborne/airborne synthetic aperture radar technology for advanced modes, real-time signal processing, and multifunctional radar imaging.

Robert Wang (M'07–SM'12) received the B.S. degree in control engineering from the University of Henan, Kaifeng, China, in 2002, and the Dr.Eng. degree from the Graduate University of Chinese Academy of Sciences, Beijing, China, in 2007.

In 2007, he joined the Center for Sensorsystems (ZESS), University of Siegen, Siegen, Germany. He has been involved in the many joint projects, supported by ZESS and Fraunhofer-FHR, e.g., TerraSAR-X/PAMIR hybrid bistatic SAR experiment, PAMIR/stationary bistatic SAR experiment, PAMIR/stationary bistatic SAR experiment with non-synchronized oscillator, and millimeter-wave FMCW SAR data processing. Since 2011, he has been a Research Fellow with the Spaceborne Microwave Remote Sensing System Department, Institute of Electronics, Chinese Academy of Sciences, Beijing, where his research has been funded by "100 Talents Programme of the Chinese Academy of Sciences." His current research interests include monostatic and multistatic SAR imaging and high-resolution spaceborne SAR system and imaging model.

Dr. Wang has been the co-Principal Investigator for Helmholtz-CAS Joint Research Group concerning Space-borne Microwave Remote Sensing for Prevention and Forensic Analysis of Natural Hazards and Extreme Events since 2012. He is responsible for several National high-resolution spaceborne imaging radar projects supported by the National High-Resolution Earth Observation Major Special Programme. He has contributed to invited sessions at the European Conference on Synthetic Aperture Radar (EUSAR) 2008–2016, the European Radar Conference 2009, and IEEE International Geoscience and Remote Sensing Symposium (IGARSS) 2012–2016. He has been chosen as the Session Chair at EUSAR 2012–2016 and IGARSS 2012–2016. He has been awarded by "National Ten Thousand Talent Program-Young Top-Notch Talent Program," "National Natural Science Funds of China for Excellent Young Scholar" in 2014, and received the "Zhao Jiuzhang Award for outstanding Young Science" in 2015.

Ning Li (S'15–M'16) received the B.S. degree in electronics information engineering from Northeast Forestry University, Harbin, China, in 2009, the M.S. degree in communication and information system from Nanjing University of Aeronautics and Astronautics, Nanjing, China, in 2012, and the Ph.D. degree in communication and information system from the University of Chinese Academy of Sciences, Beijing, China, in 2015.

Since July 2015, he has been an Assistant Professor at the Institute of Electronics, Chinese Academy of Sciences, Beijing. His research interests include synthetic aperture radar (SAR) and inverse SAR imaging algorithms and autofocusing techniques, SAR polarimetric theory, and SAR image analysis of natural hazards and extreme events.

Dr. Li received the Special Prize of President Scholarship for Postgraduate Students from the University of Chinese Academy of Sciences in 2015.

Wei Xu was born in Suzhou, China, in 1983. He received the M.S. degree from Nanjing Research Institute of Electronics Technology, Nanjing, China, in 2008, and the Ph.D. degree in communication and information engineering from the Graduate University of Chinese Academy of Sciences, Beijing, China.

Since 2011, he has been with the Spaceborne Microwave Remote Sensing System Department, Institute of Electronics, Chinese Academy of Sciences, Beijing. His research interests include spaceborne/airborne synthetic aperture radar (SAR) technology for advanced modes, SAR raw signal simulation, and SAR signal processing.

Dr. Xu received the Special Prize of President Scholarship for Postgraduate Students from the Graduate University of Chinese Academy of Sciences in 2011.

Zhen Xu received the B.S. degree from Ocean University of China, Qingdao, China, in 2012. She is currently working toward the Ph.D. degree with the Department of Space Microwave Remote Sensing System, Institute of Electronics, Chinese Academy of Sciences, Beijing, China.

She is also with the University of Chinese Academy of Sciences, Beijing. Her research interests include synthetic aperture radar image processing and imaging algorithms.